Spider peptide toxin HwTx-IV engineered to bind to lipid membranes has an increased inhibitory potency at human voltage-gated sodium channel hNa $_V$1.7

Akello J. Agwa, Nicole Lawrence, Evelyne Deplazes, Olivier Cheneval, Rachel Chen, David J. Craik, Christina I. Schroeder, Sónia T. Henriques

PII: S0005-2736(17)30028-7
DOI: doi:10.1016/j.bbamem.2017.01.020
Reference: BBAMEM 82402

To appear in: *BBA - Biomembranes*

Received date: 20 October 2016
Revised date: 3 January 2017
Accepted date: 19 January 2017

Please cite this article as: Akello J. Agwa, Nicole Lawrence, Evelyne Deplazes, Olivier Cheneval, Rachel Chen, David J. Craik, Christina I. Schroeder, Sónia T. Henriques, Spider peptide toxin HwTx-IV engineered to bind to lipid membranes has an increased inhibitory potency at human voltage-gated sodium channel hNa$_V$1.7, *BBA - Biomembranes* (2017), doi:10.1016/j.bbamem.2017.01.020

Spider peptide toxin HwTx-IV engineered to bind to lipid membranes has an increased inhibitory potency at human voltage-gated sodium channel $hNa_V1.7$

Akello J. Agwa[a], Nicole Lawrence[a], Evelyne Deplazes[a,b], Olivier Cheneval[a], Rachel Chen[a], David J. Craik[a], Christina I. Schroeder[a,]*, Sónia T. Henriques[a]*

[a] Institute for Molecular Bioscience, The University of Queensland, Qld, 4072, Australia

[b] School of Chemistry and Molecular Biosciences, The University of Queensland, Qld, 4072, Australia

E.D. current address: School of Biomedical Sciences, Curtin University, WA, 6109, Australia

* To whom correspondence should be addressed:

Dr Sónia Troeira Henriques

Institute for Molecular Bioscience

The University of Queensland

QLD, 4072, Australia

Tel: +61 7 334 62026

E-mail: s.henriques@uq.edu.au

Dr Christina I. Schroeder

Institute for Molecular Bioscience

The University of Queensland

QLD, 4072, Australia

Tel: +61 7 334 62021

E-mail: c.schroeder@imb.edu.au

Abstract

The human voltage-gated sodium channel sub-type 1.7 ($hNa_V1.7$) is emerging as an attractive target for the development of potent and sub-type selective novel analgesics with increased potency and fewer side effects than existing therapeutics. HwTx-IV, a spider derived peptide toxin, inhibits $hNa_V1.7$ with high potency and is therefore of great interest as an analgesic lead. In the current study we examined whether engineering a HwTx-IV analogue with increased ability to bind to lipid membranes would improve its inhibitory potency at $hNa_V1.7$. This hypothesis was explored by comparing HwTx-IV and two analogues [E1PyrE]HwTx-IV (mHwTx-IV) and [E1G,E4G,F6W,Y30W]HwTx-IV (gHwTx-IV) on their membrane-binding affinity and $hNa_V1.7$ inhibitory potency using a range of biophysical techniques including computational analysis, NMR spectroscopy, surface plasmon resonance, and fluorescence spectroscopy. HwTx-IV and mHwTx-IV exhibited weak affinity for lipid membranes, whereas gHwTx-IV showed improved affinity for the model membranes studied. In addition, activity assays using SH-SY5Y neuroblastoma cells expressing $hNa_V1.7$ showed that gHwTx-IV has increased activity at $hNa_V1.7$ compared to HwTx-IV. Based on these results we hypothesize that an increase in the affinity of HwTx-IV for lipid membranes is accompanied by improved inhibitory potency at $hNa_V1.7$ and that increasing the affinity of gating modifier toxins to lipid bilayers is a strategy that may be useful for improving their potency at $hNa_V1.7$.

Highlights

- gHwTx-IV, an analogue of HwTx-IV, shows increased membrane binding.
- Interactions between gHwTx-IV and the membrane appear to be electrostatic.
- Increased membrane binding is accompanied by increased potency at $hNa_V1.7$.

Keywords: drug design; peptide-membrane interactions; venom peptide; huwentoxin; pain therapeutic; gating modifier toxin

Abbreviations

BSA, bovine serum albumin; CHOL, cholesterol; C1P, ceramide-1-phosphate; $FLIPR^{TETRA}$, fluorescence imaging plate reader; GMT, gating modifier toxin; HBS, HEPES buffered saline; ICK, inhibitory cystine knot; LUV, large unilamellar vesicle; hNa_V, human voltage-gated sodium channel; POPC, 1-palmitoyl-2-oleoyl-sn-glycero-3-phosphocholine; POPS, 1-palmitoyl-2-oleoyl-sn-glycero-3-phospho-L-serine; PSS, physiological salt solution; SAR, structure-activity relationship; SM, sphingomyelin; SPR, surface plasmon resonance; SUV, small unilamellar vesicle; TFA, trifluoroacetic acid; TIPS, triisopropylsaline.

1. Introduction

There is a compelling need to improve currently available therapies for severe and chronic pain [1, 2]. Voltage-gated ion channels located on sensory neurons are involved in the transmission of pain signals to the central nervous system for interpretation and response. Some sub-types of the human voltage-gated sodium channels (hNa_VS), including the sub-type 1.7 ($hNa_V1.7$), have been linked to pain [3, 4]. Loss of function mutations on SCN9A, the gene encoding $hNa_V1.7$, result in unresponsiveness to pain, whereas gain of function mutations result in increased chronic and acute pain sensations [3, 4]. Because of this link to pain, efforts to identify potent and selective inhibitors of $hNa_V1.7$ are underway [5-8].

Peptide toxins isolated from spider venoms have shown promising potency for inhibiting $hNa_V1.7$ and therefore have potential as therapeutic leads [9]. Most of these toxins modify the kinetics and gating behavior of voltage-gated ion channels and alter the relative stability of the closed, open or inactivated states of the channels. The peptide toxins are thus classified as gating modifier toxins (GMTs) [10].

GMTs typically have a conserved amino acid arrangement resulting in a surface profile comprising a hydrophobic patch surrounded by a ring of charged residues (Figure 1B) [9, 11]. Structure activity relationship studies between the toxins and their target channels reveal that this surface motif appears to be involved in the binding of GMTs to target residues on the voltage-gated ion channels and that these peptides recognize overlapping target residues on the channels [12-14]. For example, the channel binding region of ProTx-II has been determined to bind to F813, D816 and E818 on $hNa_V1.7$, whereas HwTx-IV has been shown to interact with E811, L814, D816, E818 on the same channel [15, 16]. This raises the possibility that the toxins, rather than recognizing specific channel residues, identify a local binding site on the voltage sensor domain that is structurally and chemically complementary to the surface motif of the GMTs [12, 17].

ProTx-II is an example of a GMT whose inhibitory activity has been suggested to be dependent on ability of the peptide to bind to lipid membranes [18]. This mechanistic suggestion is based on studies showing that ProTx-II analogues with reduced or no binding affinity to lipid membranes were shown to be inactive against $hNa_V1.7$ whereas native ProTx-II, a potent inhibitor of $hNa_V1.7$ (IC_{50} = 0.3 nM) showed affinity for lipid membranes [18]. Interestingly, HwTx-IV, despite showing a high potency at $hNa_V1.7$ (IC_{50} = 27 nM), binds poorly to tested model membranes [19]. In the current study we examined whether

engineering a HwTx-IV analogue with increased ability to bind to lipid membranes would improve its inhibitory potency at $hNa_V1.7$ (Figure 1C). Biophysical studies were used to characterize peptide–membrane binding on model membranes and inhibitory potency at $hNa_V1.7$ was studied using bioassays on SH-SY5Y neuroblastoma cells. The combined results showed that increasing the membrane binding affinity of HwTx-IV also increased the inhibitory potency of the peptide toxin and these insights have the potential for translation to the design of analgesic inhibitors of $hNa_V1.7$.

2. Materials and methods

2.1. Peptide synthesis and folding

HwTx-IV, mHwTx-IV and gHwTx-IV (Figure 1C), were synthesized on a rink-amide resin at a scale of 0.25mmol to produce C-terminal amidated peptides employing standard automated 9-fluorenylmethoxycarbonyl (FMOC) solid phase peptide synthesis (SPPS) using a Symphony peptide synthesizer (Protein Technologies Inc). The peptides were cleaved from the resin with simultaneous removal of side chain protecting groups by incubation with trifluoroacetic acid (TFA)/triisopropylsilane (TIPS)/water (48:1:1) (v/v/v) for 2.5 h. The resin was filtered and TFA was evaporated under vacuum prior to precipitation with ice-cold diethyl ether. The peptides were then extracted in 45% acetonitrile (ACN) (v/v) containing 0.05% TFA (v/v)) and lyophilized. The reduced peptides were purified by reversed phase high-performance liquid chromatography (RP-HPLC) on a linear gradient of 5–55% solvent B (90% v/v ACN; 0.05% v/v TFA) over 50 min at 50 mL/min. Fractions were collected and analyzed using ESI-MS and fractions of interest were pooled, lyophilized and stored at –20 °C.

HwTx-IV and mHwTx-IV were oxidized overnight at room temperature at a concentration of 0.1 mg/mL in 0.1 M Tris-HCl (pH 8), 0.1 M NaCl, 5 mM reduced glutathione and 0.5 mM oxidized glutathione [20]. Oxidation reactions were monitored using LC/MS and quenched with solvent A (0.05% v/v TFA) to 1:2 (v/v). gHwTx-IV was dissolved in 50% v/v ACN prior to drop-wise addition to a buffer consisting of 0.1 M Tris-HCl, 10% v/v filtered isopropanol (pH 8), 5 mM reduced glutathione and 1 mM oxidized glutathione bringing the final peptide concentration to 0.05 mg/mL. The reaction was quenched by lowering the pH to pH 2 using ACN/TFA/water (1:1:1) (v/v/v) [21].

Oxidized peptides were purified using a linear gradient of 10–70% solvent B over 60 min at 8 mL/min and further separated at 3 mL/min on a gradient of 20–50% solvent B over 60 min. Fractions were collected and analyzed by ESI-MS. Fractions containing the molecular mass corresponding to the oxidized peptide were pooled, lyophilized and stored at –20 °C.

Peptide samples were quantified by absorbance at 280 nm using Nanodrop. Extinction coefficients (ε_{280}) of each peptide were calculated from the contribution of aromatic residues and disulfide bonds of the GMTs as follows: HwTx-IV ε_{280} = 7365 $M^{-1}.cm^{-1}$, mHwTx-IV ε_{280} = 7330 $M^{-1}.cm^{-1}$ and gHwTx-IV ε_{280} = 17430 $M^{-1}.cm^{-1}$.

2.2. NMR spectroscopy

HwTx-IV, mHwTx-IV and gHwTx-IV were dissolved in 90% (v/v) H_2O and 10% (v/v) D_2O to a concentration of ~1mg/mL at pH ~4. Experiments, including one-dimensional (1D) ^1H spectra and two-dimensional (2D) total correlated spectroscopy (TOCSY) (80 ms mixing time) and nuclear Overhauser effect spectroscopy (NOESY) (200 ms mixing time) were acquired on a Bruker Avance 600 MHz nuclear magnetic resonance (NMR) spectrometer equipped with a cryoprobe at 298 K to confirm correct folding of the peptides. Spectra were processed using TopSpin (Bruker), referenced to water at 4.76 ppm, and the peptide sequences were sequentially assigned using CCPNMR Analysis 2.4.1 [22, 23].

Additional NMR data were collected for the solution structure determination of gHwTx-IV, including ^1H-^{13}C HSQC and ^1H-^{15}N HSQC spectra in 90% (v/v) H_2O and 10% (v/v) D_2O in addition to TOCSY, NOESY and exclusive correlation spectra (E.COSY) spectra in 100% D_2O. Amine proton temperature coefficients were derived from a series of TOCSY experiments run on a Bruker 500 MHz NMR spectrometer in 5 K increments (283–308 K). Manually assigned intra-residue and sequential NOEs for gHwTx-IV were used to generate a list of inter-proton distances using the AUTO function in CYANA 3.97 [24]. Several rounds of AUTO calculations were used to refine peak assignments. Constraints for ϕ and φ backbone dihedral angles were generated with TALOS-N using Hα, Cα, Cβ, HN chemical shifts derived from NOESY, ^1H-^{13}C HSQC and ^1H-^{15}N HSQC spectra [25]. H-bond restraints derived from temperature coefficient experiments and D_2O exchange experiments and $\chi 1$ side chain dihedral angle restraints derived from E.COSY in combination with NOE intensities were included in structure calculations using the

ANNEAL function in CYANA. Protocols in the RECOORD database were used in CNS to calculate 50 structures, which were further refined in a water shell [26, 27]. A final set of 20 structures was then chosen based on the lowest energy, fewest violations, and the best MolProbity scores and submitted to the Protein Data Bank (PDB ID: 5TLR) and the Biomagnetic Resonance Data Bank (BMRB: 30190) (Table 1) [28].

2.3. Molecular modelling of HwTx-IV and gHwTx-IV

Solvent accessible surface area (SASA), residual dipole moments and electrostatic surface potentials of HwTx-IV and gHwTx-IV were calculated and analysed using the following molecular modelling tools. Polar and apolar SASA of the GMTs was calculated on GetArea using the default 1.4 Å water probe [29]. As HwTx-IV and gHwTx-IV are charged molecules, the dipole of these molecules is not formally defined and any calculated dipole is dependent on the translation or rotation of the peptides with respect to the origin. To facilitate a qualitative comparison between HwTx-IV and gHwTx-IV, the residual dipole moment, which is independent of position or rotation in space [30], was used. The residual dipole moment of HwTx-IV and gHwTx-IV was calculated using the g_dipoles tool on GROMACS version 5.1.12 in which the net charge is subtracted at the center of mass of the peptides [31]. Electrostatic surface potentials were calculated by solving the linearized Poisson-Boltzmann equation using the APBS software [32]. The PDB files of HwTx-IV (PDB ID: 2M4X) and gHwTx-IV (PDB ID: 5TLR) were processed using the PDB2PQR online server with the AMBER force field [33], and ProPka was used to assign protonation states of the side chains at a pH of 7.4 [27]. The electrostatic surface potential was visualized using the APBS plugin on PyMOL [34, 35].

2.4. Preparation of lipid vesicles

Synthetic 1-palmitoyl-2-oleoyl-sn-glycero-3-phosphocholine (POPC), 1-palmitoyl-2-oleoyl-sn-glycero-3-phospho-L-serine (POPS), ceramide-1-phosphate (C1P) and sphingomyelin (SM) were obtained from Avanti Polar Lipids. Synthetic cholesterol (CHOL) was obtained from Sigma Aldrich. Lipids were dissolved in spectroscopic grade chloroform and the required amounts combined to obtain mixtures of POPC, POPC/POPS (4:1 molar ratio) POPC/SM/CHOL (2.7:4:3.3 molar ratio), or POPC/C1P/CHOL (2.7:4:3.3 molar ratio). Lipid films were dried under a stream of N_2 and left *in vacuo* overnight to remove any remaining solvent. The lipid films were re-suspended in HEPES buffered saline (HBS) (10 mM HEPES,

150 mM NaCl, pH 7.4), submitted to eight freeze-thaw cycles and extruded through 50 nm or 100 nm pore sized polycarbonate filters to obtain small unilamellar vesicles (SUVs) or large unilamellar vesicles (LUVs) respectively. SUVs were used for the surface plasmon resonance (SPR) studies as their small radii facilitate the formation of lipid bilayers when deposited onto the L1 SPR sensor chip. LUVs were used for fluorescence experiments as their large radii create a more planar surface to mimic the physiological lipid bilayers [36, 37].

2.5. Peptide–membrane kinetic and affinity studies using SPR

SPR was used to examine peptide–membrane binding kinetics and affinity. Experiments were conducted at 25 °C using a Biacore 3000 instrument and an L1 sensor chip. HBS was used to prepare the peptide and lipid samples and as running buffer. Lipid bilayers were deposited onto the surface of the L1 sensor chip for 2600 s at a flow rate of 2 μL/min as previously described [18]. Peptide samples (concentrations ranging from 0–64 μM) were injected over the lipid surface for 180 s at a flow rate of 5 μL/min for the association phase. The dissociation phase lasted 600 s per injection cycle. Data were corrected for buffer contribution and normalized by assuming that 1 response unit (RU) = 1 pg/mm^2 of lipid deposited, and subsequent peptide binding as previously described [38]. Peptide–lipid membrane binding was analysed using non-linear regression one-site specific binding curves on Prism 7. Binding kinetics were studied by fitting the data of peptides at 32 μM to association then dissociation curves based on the 1:1 Langmuir model [39].

2.6. Peptide–membrane binding followed by Trp fluorescence

The peptides used in this study are intrinsically fluorescent due to the presence of Trp residue(s) in their sequences. Trp fluorescence emission spectra were therefore used to examine whether the Trp residue(s) of the peptides insert into the lipid bilayers [40]. Peptides and L-Trp (12.5 μM in HBS) were titrated with POPC/POPS (4:1) LUV suspensions to attain final lipid concentrations ranging from 0–4 mM. Fluorescence emission spectra were obtained upon excitation at 280 nm using a Perkin Elmer luminescence LS spectrometer with slits set to 3/3 nm. Peptide spectra were corrected for dilution due to titration with LUV suspensions and blanks were subtracted to examine changes in Trp fluorescence quantum yield.

Spectra were normalized to the maximum fluorescence emission intensity to delineate a potential blue shift in fluorescence emission.

To examine whether the peptide Trp residues are solvent exposed when the peptides are in the presence or absence of LUVs, samples of GMTs or L-Trp (12.5 μM in HBS) with or without 1 mM POPC/POPS (4:1) LUVs were titrated with acrylamide, an aqueous quencher, in concentrations ranging from 0–100 mM. Fluorescence emission intensity, upon excitation at 290 nm and emission at the wavelength at which the sample showed maximum emission (around 350 nm), was followed upon titration with acrylamide [40]. Data were corrected for dilution by titration with acrylamide and for dispersion from the lipid analysed using the Stern-Volmer equation [40].

2.7. Inhibition of hNa$_V$1.7 induced by HwTx-IV and its analogues

The inhibitory potency of HwTx-IV and two analogues on hNa$_V$1.7 was assessed using a calcium assay on a Fluorimetric Imaging Plate Reader (FLIPR^{TETRA}) assay as previously described [41]. SH-SY5Y cells expressing hNa$_V$1.7 were maintained in RPMI medium supplemented with 15% (v/v) fetal bovine serum (FBS), 100 units/mL penicillin, 100 units/mL streptomycin and 2 mM L-glutamine, with subculturing every 72 h (70–80% confluence).

SH-SY5Y cells were plated onto 96 well black-walled Corning™ imaging plates at a density of 65,000 cells/well 72 h prior to FLIPR ^{TETRA} assays. Immediately prior to assays, media was removed and cells were washed in physiological salt solution (PSS: 140 mM NaCl, 11.5 mM glucose, 5.9 mM KCl, 1.4 mM $MgCl_2$, 1.2 mM NaH_2PO_4, 5 mM $NaHCO_3$, 1.8 mM $CaCl_2$ and 10 mM HEPES, pH 7.4). The SH-SY5Y cells were then incubated for 30 min at 37 °C with FLIPR calcium 4 dye, 30 nM of OD1 (a selective modulator of hNa$_V$1.7 inactivation), and 0.1% (w/v) bovine serum albumin (BSA) diluted in PSS buffer as previously described [41]. Peptides were prepared to achieve final concentrations ranging from 3 μM to 1.7 × 10^{-5} μM in PSS with 0.1% (w/v) BSA. The Na$_V$1.7 agonist, veratridine, was prepared to achieve a final concentration of 4 μM in PSS with 0.1% (w/v) BSA. Test peptides were added to the cells and incubated for an additional 15 min using the FLIPR^{TETRA} instrument at 25 °C. Fluorescence emission intensity (excitation 470–495 nm; emission 515–575 nm) was recorded every second for ten initial baseline reads, followed by the addition of veratridine. Fluorescence emission intensity (a measure of calcium influx into the cells

following veratridine activation of $hNa_V1.7$) was then recorded every second for 300 s and the raw data were corrected for the contribution of buffer and transformed to maximal response over baseline using Screenworks 3.1.1.4 (Molecular Devices). Data were normalized to the maximal change in fluorescence emission for each peptide prior to analysis on Prism 7 using one-site specific binding with Hill slope and Bmax = 1.

3. Results

The purpose of this study was to determine whether increasing the membrane binding properties of HwTx-IV would increase its inhibitory at $hNa_V1.7$. To achieve this goal, two analogues of HwTx-IV, [EPyrE]HwTx-IV (mHwTx-IV) and [E1G,E4G,F6W,Y33W]HwTx-IV (gHwTx-IV), were studied (Figure 1C). mHwTx-IV is a naturally occurring derivative of HwTx-IV characterized by a post-translational modification conferring a pyroglutamic acid (PyrE) residue at position 1. The E1PyrE modification on mHwTx-IV has been determined previously to result in a longer duration of inhibition of $hNa_V1.7$ [42]. gHwTx-IV is a derivative of another HwTx-IV analogue: [E1G,E4G,Y33W]HwTx-IV, shown previously to have increased potency at $hNa_V1.7$ (IC_{50} = 0.4 nM) compared to HwTx-IV (IC_{50} = 27 nM) [21].

3.1. Peptide synthesis and NMR analyses on HwTx-IV, mHwTx-IV and gHwTx-IV

All peptides in this study were successfully synthesized and oxidized with final yields of > 90% for HwTx-IV and mHwTx-IV and approximately 10% for gHwTx-IV. 1D ^{1}H and 2D TOCSY and NOESY spectra were obtained for HwTx-IV, mHwTx-IV and gHwTx-IV. All peptides were confirmed to be folded as was evidenced by well dispersed peaks in the amide region (7–10 ppm) of the 1D ^{1}H spectra. TOCSY and NOESY spectra were then used for the successful sequential assignment of individual amino acid spin systems [23]. Hα chemical shifts were used to compare mHwTx-IV and gHwTx-IV to native HwTx-IV. Overall, there were minimal chemical shift differences except at, or near positions on mHwTx-IV and gHwTx-IV where sequence modifications were present (Figure 2A). This observation indicated that the three synthetic peptides have similar overall structures and the same disulfide connectivity.

The NMR solution structure of gHwTx-IV was calculated and refined using CYANA and CNS. The 20 final structures were based on 395 distance restraints, including 130 intraresidue, 134 sequential, 36

medium range ($|i - j| < 5$), 90 long range ($|i - j| > 5$ and 10 hydrogen bond distance restraints. In addition, 42 dihedral angle restraints composing 18 ϕ, 19 φ and 5 $\chi 1$ angle restraints were included (Table 1). The final 20 structures were selected based on low overall energies, two or fewer violations from experimental restraints, and satisfactory MolProbity scores (Figure 2B). The 20 conformers were superimposed and gave an overall global backbone RMSD of 0.99 ± 0.34 Å and a global heavy RMSD of 1.72 ± 0.38 Å. Not including the flexible N- and C-termini (residues 1 and 32-35), global backbone RMSD was 0.59 ± 0.13 Å and global heavy RMSD was 1.34 ± 0.17 Å (Table 1). The solution structure of gHwTx-IV was characterised by an ICK motif typical of spider derived GMTs [9]. The ICK structure featured loops and turns as well a pair of short antiparallel beta sheets between residues 23–24 and 31–32; features common to ICK peptides [43].

3.2. Peptide–lipid bilayer kinetic and affinity studies using SPR

Peptide–lipid bilayer interactions of HwTx-IV and its analogues were studied using SPR and model membranes of varying charge and fluidity. Choice of model membranes in this study was based on features of the eukaryotic cell membrane, which exists as a heterogeneous fluid bilayer. Phospholipids containing a phosphatidylcholine headgroup are the most abundant lipids in eukaryotic cell membranes, thus vesicles composed of POPC, which forms zwitterionic fluid model membranes at 25 °C, were used as an initial simple model membrane [44]. Negatively-charged vesicles composed of POPC/POPS (4:1) were used to examine the importance of electrostatic interactions between the peptide and the membrane and to mimic the effect of having negatively-charged molecules at the cell surface. Although the lipids that compose the outer leaflet of the cell membrane are primarily neutrally charged, there are anionic molecules present in the outer leaflet of physiological membranes [44] (e.g. extracellular regions of Na_V channels and proteoglycans that possess a serine to which glycosaminoglycan chains are attached to [45]). The membrane environments in the vicinity of ion channels are proposed to have lipids arranged in domains (rafts) whose compositions typically have high proportions of CHOL and SM; furthermore, studies have shown that the venoms of some spiders have enzymes that drive the conversion of SM to the anionic ceramide-1-phosphate (C1P) [46, 47]. Therefore, the neutrally charged, POPC/SM/CHOL (2.7:4:3.3) and anionic POPC/C1P/CHOL (2.7:4:3.3 molar ratio) model membranes were also studied [48, 49].

The SPR data showed that gHwTx-IV has higher affinity and binding maxima in the four model membranes studied when compared to HwTx-IV and mHwTx-IV (Figure 3A, B). Furthermore, gHwTx-IV had preferential interactions (higher binding maxima and slower dissociation-rates) with the anionic POPC/POPS (4:1) and POPC/C1P/CHOL (2.7:4:3.3), in comparison to neutral POPC and POPC/SM/CHOL (2.7:4:3.3) model membranes (Table 2).

3.3. In-depth location of peptide Trp residues within the lipid membrane

Fluorescence emission of Trp residues on peptides is sensitive to the surrounding environment; thus Trp fluorescence emission properties of peptides in the presence and absence of model membranes can be used to examine whether Trp residues are involved in the interaction between the peptide and the lipid membrane. The Trp fluorescence emission profile of gHwTx-IV and HwTx-IV was followed upon titration with LUV suspensions. Whereas the Trp fluorescence emission profile of HwTx-IV did not change upon titration with POPC/POPS (4:1) vesicles, there was a blue shift of 7 nm with no considerable change in the quantum yield in the fluorescence emission spectra of gHwTx-IV upon titration with lipid vesicles to a concentration of 4 mM (Figure 3C). These results show that in the presence of lipid, the Trp residues on gHwTx-IV become less exposed to the aqueous environment, and suggest that the residues are involved in the binding of the peptide to the lipid bilayer.

Acrylamide is a water-soluble quencher of fluorescence emission from Trp residues on peptides and is unable to partition into lipid bilayers and thus can only efficiently quench fluorescence emission of Trp residues that are aqueous exposed. When Trp residues on peptides insert into lipid membranes they are protected from acrylamide quenching; therefore, the Trp fluorescence quenching efficiency by acrylamide in the presence of lipid vesicles was examined to give information on the position of the Trp residues when the peptides interact with lipid bilayers. The quenching efficiency of acrylamide was compared using the Stern Volmer constant (K_{SV}) [37, 40]. Acrylamide efficiently quenched the fluorescence emission of the Trp residues of HwTx-IV and gHwTx-IV in buffer suggesting that the Trp residues of the peptides are solvent exposed and not buried in the core of the peptide structures. The acrylamide quenching of the Trp residue on HwTx-IV (K_{SV} = 48.4 ± 1.2 M^{-1}) was comparable to the negative control (L-Trp) (K_{SV} = 49.1 ± 2.5 M^{-1}) in the presence of 1 mM POPC/POPS (4:1) LUVs supporting the observation that HwTx-IV does not insert

into the membrane. Acrylamide was a less efficient quencher of the Trp fluorescence emission of gHwTx-IV in the presence of POPC/POPS (4:1) LUVs (K_{SV} = 37.5 ± 1.5 M^{-1}) than in buffer (K_{SV} = 44.1 ± 2.0 M^{-1}) (Figure 3D). The small difference in K_{SV} values suggests that the Trp residues in gHwTx-IV have a shallow position when bound to lipid membranes such that the residues are still accessible to acrylamide.

3.4. Comparison of charge and surface properties of HwTx-IV and gHwTx-IV

To examine the features that confer gHwTx-IV with the ability to interact with lipid bilayers, we compared the net charge, residual dipole moment, solvent accessible surface area (SASA), electrostatic surface potentials and chemical surface profiles of gHwTx-IV and HwTx-IV. It can be expected that mHwTx-IV would show similar surface properties to HwTx-IV given the overall similarity in their structures based on secondary Hα shifts, and the only charge difference being the absence of a Glu residue at position 1 (Figure 2A). gHwTx-IV, on the other hand, has a higher net charge (+6 compared to +4 for HwTx-IV) as well as a higher residual dipole moment and more apolar SASA than HwTx-IV (Table 3). A surface profile comparison showed that gHwTx-IV had a larger hydrophobic surface area than HwTx-IV (Figure 5A). Furthermore, a comparison of the GMT electron density distributions showed that the surface of gHwTx-IV possessing the mutations was more positive than the same surface on HwTx-IV (Figure 5B). These results are attributable to the replacement of the anionic E1, E4, with the apolar G1, and G4 and the replacement of F6, Y33 more hydrophobic W6 and W33.

3.5. Inhibitory activity of HwTx-IV, mHwTx-IV and gHwTx-IV at hNa$_V$1.7

To determine whether gHwTx-IV, the analogue that showed increased lipid bilayer interactions, would also show increased inhibitory activity at hNa$_V$1.7, the FLIPR calcium 4 assay was performed using SH-SY5Y neuroblastoma cells as previously described [41]. The three peptides slowed down the activation kinetics of hNa$_V$1.7 (Figure 4A). HwTx-IV (IC_{50} = 32.4 ± 4.7 nM) and mHwTx-IV (IC_{50} = 30.8 ± 5.2 nM) had similar inhibitory activity; whereas gHwTx-IV showed an increase in inhibitory potency (IC_{50} = 7.6 ± 1.5 nM) at hNa$_V$1.7 (Figure 4B).

4. Discussion

The structures of GMTs isolated from spiders are typically characterized by a conserved hydrophobic patch surrounded by a charged ring. This structural feature has been proposed to promote not only GMT–voltage-gated ion channel interactions, but also GMT–lipid membrane interactions [12, 13, 17, 18, 48]. Several spider GMTs have been shown to interact with model membranes and the unique structures of these peptides have been proposed to facilitate a tri-molecular interaction involving the GMTs, the lipid membrane and target voltage-gated ion channels [14, 47, 50-52]. HwTx-IV is a potent inhibitor of $hNa_V1.7$; however, this GMT has been reported to have a weak affinity for lipid membranes [16, 19]. In this study we confirm that HwTx-IV has weak membrane affinity and we compare the peptide to two analogues, mHwTx-IV and gHwTx-IV. Results from membrane binding studies and activity assays show that mHwTx-IV has similar weak membrane binding interactions to HwTx-IV and a nearly identical inhibitory potency at $hNa_V1.7$. In contrast, gHwTx-IV simultaneously displays increased inhibitory activity at $hNa_V1.7$ and increased interactions with lipid membranes.

Peptide–lipid membrane interactions were studied in fluid and raft-like model membranes of both anionic and zwitterionic overall charges. In comparison to HwTx-IV and mHwTx-IV, which showed similar weak interactions with the model membranes, gHwTx-IV consistently showed the highest affinity to all model membranes tested (Figure 3A, B). Furthermore, acrylamide quenching of the fluorescence emission of Trp residues on the peptides suggested that gHwTx-IV adopts a superficial position on the membrane (Figure 3D). This position on the membrane surface is likely to be facilitated by a combination of electrostatic, hydrogen bonding and hydrophobic interactions between the peptide and the phospholipid headgroups of the lipid membrane. Several prior GMT–membrane binding studies have proposed that the hydrophobic patch present on these spider toxins is important for hydrophobic interactions with the membrane and that the charged ring of these spider derived peptides participates in electrostatic interactions with the phospholipid headgroups [18, 53-55]. The importance of electrostatic interactions between gHwTx-IV and the lipid membrane is supported by the observation that gHwTx-IV has a higher affinity for anionic lipid membranes (Figure 3 A, B). Furthermore, a global profile of the electrostatic surface potential on the surface of gHwTx-IV containing the four mutations (E1G, E4G, F6W and Y33W) is more positive than the

same surface on HwTx-IV (Figure 5B), and gHwTx-IV has a higher net charge and residual dipole moment than HwTx-IV (Table 3). Together these features can promote GMT electrostatic interactions with the phospholipid headgroups of the membrane. The interactions between gHwTx-IV and the lipid membrane are likely also facilitated by hydrogen bonding between the indole groups on the side chains of W6 and W33, and the phospholipid headgroups of the membrane. Additionally, hydrophobic interactions could also play a role in the gHwTx-IV–lipid membrane interaction as is evidenced from the findings that gHwTx-IV has a larger hydrophobic patch (Figure 5A) and apolar SASA (Table 3) than HwTx-IV.

In addition to increased membrane interactions, gHwTx-IV showed a 4-fold increase in inhibition of $hNa_V1.7$ compared to both HwTx-IV and mHwTx-IV, which had similar inhibitory potencies. In a previous structure-activity relationship (SAR) study with an alanine scan of HwTx-IV, a region at the surface of the molecule was proposed to be responsible for the interaction with $hNa_V1.7$ [12]. Specifically, it was suggested that the amino acid residues R26, K27 and K32 on HwTx-IV interact with D816, E818 and E811 on the extracellular loop of voltage sensor domain II of $hNa_V1.7$ (Figure 6) [12]. Our studies with gHwTx-IV suggest that the combination of the mutations E1G, E4G, F6W and Y33W result in both increased membrane binding and increased inhibition of $hNa_V1.7$. These four mutations are part of a hydrophobic patch located at the surface of the molecule distinct from the surface formed by the channel binding residues R26, K27 and K32 (Figure 6A).

We propose that the increased potency observed with gHwTx-IV, compared to HwTX-IV, is facilitated by membrane-binding interactions. Briefly, electrostatic interactions between gHwTx-IV and the membrane would attract the peptide to the membrane surface and additional hydrogen bonding and hydrophobic interactions would orient the peptide such that the face containing R26, K27 and K32 is available for interactions with $hNa_V1.7$ (Figure 6). In addition, the overall decrease in anionic charge and increase in hydrophobicity of gHwTx-IV might further augment interactions between the peptide and $hNa_V1.7$ This hypothesis was previously proposed by Revell and colleagues [13], when the authors observed an increase in the inhibitory potency of the analogue [E1G,E4G,Y33W]HwTx-IV [21]. *In silico* docking studies suggested that the residues F6 and Y33 form hydrophobic interactions with M750 on $hNa_V1.7$; thus, a supporting explanation for the increased activity observed with gHwTx-IV is that the mutations F6W and

Y33W would improve the hydrophobic interaction with M750 due to the increased hydrophobic character of tryptophan compared to that of phenylalanine and tyrosine [12, 56]. Although we cannot exclude the possibility that an increased inhibitory potency on $hNa_V1.7$ and increased membrane binding are independent, we propose a model where gHwTx-IV acts by binding both to the membrane and to the target channel (Figure 6B). A similar mechanism has been suggested for ProTx-I and ProTx-II, two GMTs that also seem to possess distinct surface regions responsible for membrane interaction and for channel interaction [18, 48]. Furthermore, the fact the amino acid residues that seem to be involved in membrane binding are distinct from those involved in channel binding lead us to postulate that gHwTx-IV will show a similar selectivity profile to HwTx-IV, particularly against $Na_V1.5$ which is involved in cardiac muscle conduction [16]. This hypothesis is further supported by [E1G,E4G,Y33W]HwTx-IV, an analogue similar to gHwTx-IV, which was found to be inactive at $Na_V1.5$ [21].

We conclude that by engineering HwTx-IV to increase membrane interactions, we have simultaneously designed a peptide with higher activity at $hNa_V1.7$. Overall charge and hydrophobicity play important roles both in interactions of gHwTx-IV with $hNa_V1.7$ and with lipid membranes. Two predominant theories for GMT–membrane interactions are that the lipid bilayer acts to concentrate the peptide at the active site for the purpose of increasing peptide availability at the channel active site and secondly that GMT–membrane interactions facilitate access to the voltage sensor domain, which rests at a superficial position in the bilayer [57, 58]. The way forward is therefore to study GMTs, model membranes and channels in concert to better understanding of the mechanism of action of this tri-molecular complex, with the aim of developing peptides with higher inhibitory potency at $hNa_V1.7$.

5. Acknowledgements and author contributions

This work is supported by a grant to C.I.S and S.T.H (APP1080405) from the Australian National Health and Medical Research Council (NHMRC). S.T.H is an Australian Research Council (ARC) Future Fellow (FT150100398) and an Institute for Molecular Bioscience (IMB) Fellow, C.I.S is an IMB Industry Fellow, E.D. is a NHMRC Early Career Research Fellow (APP1071293), D.J.C is an ARC Australian Laureate Fellow (FL150100146) and A.J.A is supported by a University of Queensland International

postgraduate student scholarship. We thank Dr Irina Vetter (IMB, UQ) for providing the SH-SY5Y cells and for discussions on the FLIPR activity assay.

S.T.H, C.I.S, N.L and A.J.A designed the study. O.C. synthesized the peptides and A.J.A, O.C and R.C oxidized and purified the peptides. A.J.A and C.I.S performed and analyzed NMR experiments and calculated the three-dimensional structure of gHwTx-IV. A.J.A and S.T.H conducted and analyzed data from lipid membrane studies including surface plasmon resonance and fluorescence spectroscopy experiments. A.J.A and N.L cultured cells, conducted the FLIPR assays, on SH-SY5Y neuroblastoma cells expressing $hNa_V1.7$ and analyzed the resulting data. A.J.A and E.D. performed the *in silico* studies on the peptides. A.J.A, S.T.H, C.I.S and N.L wrote the manuscript. D.J.C critically reviewed the manuscript. All authors read the manuscript and provided specific feedback.

References

[1] D. Holmes, The pain drain, Nature, 535 (2016) S2-S3.

[2] M. Grayson, Pain, Nature, 535 (2016) S1-S1.

[3] S.D. Dib-Hajj, T.R. Cummins, J.A. Black, S.G. Waxman, From genes to pain: Nav 1.7 and human pain disorders, Trends Neurosci., 30 (2007) 555-563.

[4] A. Momin, J.N. Wood, Sensory neuron voltage-gated sodium channels as analgesic drug targets, Curr. Opin. Neurobiol., 18 (2008) 383-388.

[5] J.R. Deuis, J.S. Wingerd, Z. Winter, T. Durek, Z. Dekan, S.R. Sousa, K. Zimmermann, T. Hoffmann, C. Weidner, M.A. Nassar, P.F. Alewood, R.J. Lewis, I. Vetter, Analgesic effects of GpTx-1, PF-04856264 and CNV1014802 in a mouse model of Na(V)1.7-mediated pain, Toxins, 8 (2016) 78.

[6] J.K. Murray, J. Long, A. Zou, J. Ligutti, K.L. Andrews, L. Poppe, K. Biswas, B.D. Moyer, S.I. McDonough, L.P. Miranda, Single residue substitutions that confer voltage-gated sodium ion channel subtype selectivity in the $Na_V1.7$ inhibitory peptide GpTx-1, J. Med. Chem., 59 (2016) 2704-2717.

[7] S. Ahuja, S. Mukund, L. Deng, K. Khakh, E. Chang, H. Ho, S. Shriver, C. Young, S. Lin, J.P. Johnson, P. Wu, J. Li, M. Coons, C. Tam, B. Brillantes, H. Sampang, K. Mortara, K.K. Bowman, K.R. Clark, A. Estevez, Z. Xie, H. Verschoof, M. Grimwood, C. Dehnhardt, J.-C. Andrez, T. Focken, D.P. Sutherlin, B.S. Safina, M.A. Starovasnik, D.F. Ortwine, Y. Franke, C.J. Cohen, D.H. Hackos, C.M. Koth, J. Payandeh, Structural basis of $Na_V1.7$ inhibition by an isoform-selective small-molecule antagonist, Science (New York, N.Y.), 350 (2015) aac5464.

[8] J.H. Park, K.P. Carlin, G. Wu, V.I. Ilyin, L.L. Musza, P.R. Blake, D.J. Kyle, Studies examining the relationship between the chemical structure of protoxin II and its activity on voltage gated sodium channels, J. Med. Chem., 57 (2014) 6623-6631.

[9] J.K. Klint, S. Senff, D.B. Rupasinghe, S.Y. Er, V. Herzig, G.M. Nicholson, G.F. King, Spider-venom peptides that target voltage-gated sodium channels: pharmacological tools and potential therapeutic leads, Toxicon, 60 (2012) 478-491.

[10] W.A. Catterall, S. Cestele, V. Yarov-Yarovoy, F.H. Yu, K. Konoki, T. Scheuer, Voltage-gated ion channels and gating modifier toxins, Toxicon, 49 (2007) 124-141.

[11] F. Bosmans, K.J. Swartz, Targeting sodium channel voltage sensors with spider toxins, Trends Pharmacol. Sci., 31 (2010) 175-182.

[12] N.A. Minassian, A. Gibbs, A.Y. Shih, Y. Liu, R.A. Neff, S.W. Sutton, T. Mirzadegan, J. Connor, R. Fellows, M. Husovsky, S. Nelson, M.J. Hunter, M. Flinspach, A.D. Wickenden, Analysis of the structural and molecular basis of voltage-sensitive sodium channel inhibition by the spider toxin huwentoxin-IV (mu-TRTX-Hh2a), J. Biol. Chem., 288 (2013) 22707-22720.

[13] H.H. Jung, H.J. Jung, M. Milescu, C.W. Lee, S. Lee, J.Y. Lee, Y.-J. Eu, H.H. Kim, K.J. Swartz, J.I. Kim, Structure and orientation of a voltage-sensor toxin in lipid membranes, Biophys. J., 99 (2010) 638-646.

[14] M. Milescu, J. Vobecky, S.H. Roh, S.H. Kim, H.J. Jung, J.I. Kim, K.J. Swartz, Tarantula toxins interact with voltage sensors within lipid membranes, J. Gen. Physiol., 130 (2007) 497-511.

[15] W.A. Schmalhofer, J. Calhoun, R. Burrows, T. Bailey, M.G. Kohler, A.B. Weinglass, G.J. Kaczorowski, M.L. Garcia, M. Koltzenburg, B.T. Priest, ProTx-II, a selective inhibitor of $Na_V1.7$ sodium channels, blocks action potential propagation in nociceptors, Mol. Pharmacol., 74 (2008) 1476-1484.

[16] Y. Xiao, J.P. Bingham, W. Zhu, E. Moczydlowski, S. Liang, T.R. Cummins, Tarantula huwentoxin-IV inhibits neuronal sodium channels by binding to receptor site 4 and trapping the domain II voltage sensor in the closed configuration, J. Biol. Chem., 283 (2008) 27300-27313.

[17] T. Cai, J. Luo, E. Meng, J. Ding, S. Liang, S. Wang, Z. Liu, Mapping the interaction site for the tarantula toxin hainantoxin-IV (beta-TRTX-Hn2a) in the voltage sensor module of domain II of voltage-gated sodium channels, Peptides, 68 (2015) 148-156.

[18] E. Deplazes, S.T. Henriques, J.J. Smith, G.F. King, D.J. Craik, A.E. Mark, C.I. Schroeder, Membrane-binding properties of gating modifier and pore-blocking toxins: Membrane interaction is not a prerequisite for modification of channel gating, Biochim. Biophys. Acta, 1858 (2016) 872-882.

[19] Y. Xiao, X. Luo, F. Kuang, M. Deng, M. Wang, X. Zeng, S. Liang, Synthesis and characterization of huwentoxin-IV, a neurotoxin inhibiting central neuronal sodium channels, Toxicon, 51 (2008) 230-239.

[20] M. Deng, X. Luo, L. Jiang, H. Chen, J. Wang, H. He, S. Liang, Synthesis and biological characterization of synthetic analogs of Huwentoxin-IV (Mu-theraphotoxin-Hh2a), a neuronal tetrodotoxin-sensitive sodium channel inhibitor, Toxicon, 71 (2013) 57-65.

[21] J.D. Revell, P.E. Lund, J.E. Linley, J. Metcalfe, N. Burmeister, S. Sridharan, C. Jones, L. Jermutus, M.A. Bednarek, Potency optimization of huwentoxin-IV on hNa$_V$1.7: a neurotoxin TTX-S sodium-channel antagonist from the venom of the Chinese bird-eating spider *Selenocosmia huwena*, Peptides, 44 (2013) 40-46.

[22] W.F. Vranken, W. Boucher, T.J. Stevens, R.H. Fogh, A. Pajon, M. Llinas, E.L. Ulrich, J.L. Markley, J. Ionides, E.D. Laue, The CCPN data model for NMR spectroscopy: development of a software pipeline, Proteins, 59 (2005) 687-696.

[23] K. Wuthrich, NMR of proteins and nucleic acids, Wiley Interscience, New York, 1986.

[24] P. Guntert, Automated NMR structure calculation with CYANA, Methods Mol Biol, 278 (2004) 353-378.

[25] Y. Shen, A. Bax, Protein backbone and sidechain torsion angles predicted from NMR chemical shifts using artificial neural networks, J. Biomol. NMR, 56 (2013) 227-241.

[26] A.T. Brunger, P.D. Adams, G.M. Clore, W.L. DeLano, P. Gros, R.W. Grosse-Kunstleve, J.S. Jiang, J. Kuszewski, M. Nilges, N.S. Pannu, R.J. Read, L.M. Rice, T. Simonson, G.L. Warren, Crystallography & NMR system: A new software suite for macromolecular structure determination, Acta crystallographica. Section D, Biological crystallography, 54 (1998) 905-921.

[27] A.J. Nederveen, J.F. Doreleijers, W. Vranken, Z. Miller, C.A. Spronk, S.B. Nabuurs, P. Guntert, M. Livny, J.L. Markley, M. Nilges, E.L. Ulrich, R. Kaptein, A.M. Bonvin, RECOORD: a recalculated coordinate database of 500+ proteins from the PDB using restraints from the BioMagResBank, Proteins, 59 (2005) 662-672.

[28] I.W. Davis, A. Leaver-Fay, V.B. Chen, J.N. Block, G.J. Kapral, X. Wang, L.W. Murray, W.B. Arendall, 3rd, J. Snoeyink, J.S. Richardson, D.C. Richardson, MolProbity: all-atom contacts and structure validation for proteins and nucleic acids, Nucleic Acids Res., 35 (2007) W375-383.

[29] R. Fraczkiewicz, W. Braun, Exact and efficient analytical calculation of the accessible surface areas and their gradients for macromolecules, J. Comput. Chem, 19 (1998) 319-333.

[30] A.D. Buckingham, Molecular quadrupole moments, Q. Rev. Chem. Soc., 13 (1959) 183-214.

[31] D. Van Der Spoel, E. Lindahl, B. Hess, G. Groenhof, A.E. Mark, H.J.C. Berendsen, GROMACS: Fast, flexible, and free, J. Comput. Chem, 26 (2005) 1701-1718.

[32] T.J. Dolinsky, J.E. Nielsen, J.A. McCammon, N.A. Baker, PDB2PQR: an automated pipeline for the setup of Poisson–Boltzmann electrostatics calculations, Nucleic Acids Res., 32 (2004) W665-W667.

[33] T.J. Dolinsky, P. Czodrowski, H. Li, J.E. Nielsen, J.H. Jensen, G. Klebe, N.A. Baker, PDB2PQR: expanding and upgrading automated preparation of biomolecular structures for molecular simulations, Nucleic Acids Res., 35 (2007) W522-W525.

[34] The PyMOL Molecular Graphics System, in, Schrodinger, LLC.

[35] N.A. Baker, D. Sept, S. Joseph, M.J. Holst, J.A. McCammon, Electrostatics of nanosystems: Application to microtubules and the ribosome, Proc. Natl. Acad. Sci., 98 (2001) 10037-10041.

[36] S.T. Henriques, Y.H. Huang, M.A. Castanho, L.A. Bagatolli, S. Sonza, G. Tachedjian, N.L. Daly, D.J. Craik, Phosphatidylethanolamine binding is a conserved feature of cyclotide-membrane interactions, J. Biol. Chem., 287 (2012) 33629-33643.

[37] A.S. Ladokhin, S. Jayasinghe, S.H. White, How to measure and analyze tryptophan fluorescence in membranes properly, and why bother?, Anal. Biochem., 285 (2000) 235-245.

[38] S.T. Henriques, Y.H. Huang, K.J. Rosengren, H.G. Franquelim, F.A. Carvalho, A. Johnson, S. Sonza, G. Tachedjian, M.A. Castanho, N.L. Daly, D.J. Craik, Decoding the membrane activity of the cyclotide kalata B1: the importance of phosphatidylethanolamine phospholipids and lipid organization on hemolytic and anti-HIV activities, J. Biol. Chem., 286 (2011) 24231-24241.

[39] S.T. Henriques, L.K. Pattenden, M.-I. Aguilar, M.A.R.B. Castanho, The toxicity of prion protein fragment PrP(106−126) is not mediated by membrane permeabilization as shown by a M112W substitution, Biochemistry, 48 (2009) 4198-4208.

[40] J.R. Lakowicz, Principles of fluorescence spectroscopy, Third ed., Springer Science+Business Media, New York, NY, 2006.

[41] I. Vetter, C.A. Mozar, T. Durek, J.S. Wingerd, P.F. Alewood, M.J. Christie, R.J. Lewis, Characterisation of Nav types endogenously expressed in human SH-SY5Y neuroblastoma cells, Biochem. Pharmacol., 83 (2012) 1562-1571.

[42] M. Rong, Z. Duan, J. Chen, J. Li, Y. Xiao, S. Liang, Native pyroglutamation of huwentoxin-IV: a post-translational modification that increases the trapping ability to the sodium channel, PLoS One, 8 (2013) e65984.

[43] P.K. Pallaghy, K.J. Nielsen, D.J. Craik, R.S. Norton, A common structural motif incorporating a cystine knot and a triple-stranded beta-sheet in toxic and inhibitory polypeptides, Protein Sci., 3 (1994) 1833-1839.

[44] G. van Meer, D.R. Voelker, G.W. Feigenson, Membrane lipids: where they are and how they behave, Nat. Rev. Mol. Cell Biol., 9 (2008) 112-124.

[45] N. Perrimon, M. Bernfield, Cellular functions of proteoglycans—an overview, Semin. Cell Dev. Biol., 12 (2001) 65-67.

[46] Y. Ramu, Y. Xu, Z. Lu, Enzymatic activation of voltage-gated potassium channels, Nature, 442 (2006) 696-699.

[47] M. Milescu, F. Bosmans, S. Lee, A.A. Alabi, J.I. Kim, K.J. Swartz, Interactions between lipids and voltage sensor paddles detected with tarantula toxins, Nat. Struct. Mol. Biol., 16 (2009) 1080-1085.

[48] S.T. Henriques, E. Deplazes, N. Lawrence, O. Cheneval, S. Chaousis, M. Inserra, P. Thongyoo, G.F. King, A.E. Mark, I. Vetter, D.J. Craik, C.I. Schroeder, Interaction of tarantula venom peptide ProTx-II with lipid membranes is a prerequisite for its inhibition of human voltage-gated sodium channel $Na_V1.7$, J. Biol. Chem., (2016).

[49] R.F.M. de Almeida, A. Fedorov, M. Prieto, Sphingomyelin/phosphatidylcholine/cholesterol phase diagram: boundaries and composition of lipid rafts, Biophys. J., 85 (2003) 2406-2416.

[50] S.Y. Lee, R. MacKinnon, A membrane-access mechanism of ion channel inhibition by voltage sensor toxins from spider venom, Nature, 430 (2004) 232-235.

[51] T.M. Suchyna, S.E. Tape, R.E. Koeppe, 2nd, O.S. Andersen, F. Sachs, P.A. Gottlieb, Bilayer-dependent inhibition of mechanosensitive channels by neuroactive peptide enantiomers, Nature, 430 (2004) 235-240.

[52] J.J. Smith, S. Alphy, A.L. Seibert, K.M. Blumenthal, Differential phospholipid binding by site 3 and site 4 toxins. Implications for structural variability between voltage-sensitive sodium channel domains, J. Biol. Chem., 280 (2005) 11127-11133.

[53] D. Bemporad, Z.A. Sands, C.L. Wee, A. Grottesi, M.S. Sansom, VsTx-1, a modifier of K_V channel gating, localizes to the interfacial region of lipid bilayers, Biochemistry, 45 (2006) 11844-11855.

[54] C.L. Wee, D. Bemporad, Z.A. Sands, D. Gavaghan, M.S.P. Sansom, SgTx-1, a K_V channel gating-modifier toxin, binds to the interfacial region of lipid bilayers, Biophys. J., 92 (2007) L07-L09.

[55] Y.O. Posokhov, P.A. Gottlieb, M.J. Morales, F. Sachs, A.S. Ladokhin, Is lipid bilayer binding a common property of inhibitor cysteine knot ion-channel blockers?, Biophys. J., 93 (2007) L20-22.

[56] C.H. Luan, T.M. Parker, D.C. Gowda, D.W. Urry, Hydrophobicity of amino acid residues: differential scanning calorimetry and synthesis of the aromatic analogues of the polypentapeptide of elastin, Biopolymers, 32 (1992) 1251-1261.

[57] S.-Y. Lee, R. MacKinnon, A membrane-access mechanism of ion channel inhibition by voltage sensor toxins from spider venom, Nature, 430 (2004) 232-235.

[58] L. Revell Phillips, M. Milescu, Y. Li-Smerin, J.A. Mindell, J.I. Kim, K.J. Swartz, Voltage-sensor activation with a tarantula toxin as cargo, Nature, 436 (2005) 857-860.

[59] R. Koradi, M. Billeter, K. Wuthrich, MOLMOL: a program for display and analysis of macromolecular structures, J. Mol. Graph., 14 (1996) 51-55, 29-32.

Table 1. Energies and structural statistics for the family of 20 gHwTx-IV (PDB ID: 5TLR) structures[a].

Energies (kcal/mol)	
Overall	-990.61 ± 59.80
Bonds	25.80 ± 1.58
Angles	52.39 ± 4.77
Improper	17.46 ± 2.71
Dihedral	166.04 ± 2.33
Van der Waals	-150.46 ± 4.73
Electrostatic	-1102.63 ± 61.84
NOE	0.38 ± 0.03
Constrained dihedral (cDih)	0.39 ± 0.37
Mol Probity statistics	
Clash score (>0.4 Å / 1000 atoms)	14.05 ± 3.44
Poor rotamers	0.78 ± 1.39
Ramachandran outliers (%)	0.76 ± 1.34
Ramachandran favoured (%)	85.17 ± 2.84
MolProbity score	2.38 ± 0.28
MolProbity percentile	53.90 ± 15.03[c]
Atomic RMSD (Å)	
Mean global backbone (2–31)[d]	0.59 ± 0.13
Mean global heavy (2–31)	1.34 ± 0.17
Mean global backbone (1–35)	0.99 ± 0.34
Mean global heavy (1–35)	1.72 ± 0.38
Distance restraints	
Intraresidue ($i - j = 0$)	130
Sequential ($\|i - j\| = 1$)	134
Medium range ($\|i - j\| < 5$)	36
Long range ($\|i - j\| > 5$)	90
Hydrogen bonds[e]	10
Total	395
Dihedral angle restraints	
ϕ	18
φ	19
$\chi 1$	5
Total	42
Violations from experimental restraints	
Total NOE violations exceeding 0.2 Å	1
Total dihedral violations exceeding 2.0°	2

[a] Based on structures with highest overall MolProbity score [28].
[b] ± St Dev
[c] 100th percentile is the best among structures of comparable resolution; 0th percentile is the worst.
[d] RMSD calculated in MOLMOL [59].
[e] Two restraints were used per hydrogen bond.

Table 2. Binding affinity and dissociation rates of HwTx-IV and its analogues to model membranes as determined from SPR studies

	POPC		POPC/POPS (4:1)		POPC/SM/CHOL (2.7:4:3.3)		POPC/C1P/CHOL (2.7:4:3.3)	
Peptide	**P/Lmax [a] (mol/mol)**	**K_{off} [b] (s^{-1})**	**P/Lmax (mol/mol)**	**K_{off} (s^{-1})**	**P/Lmax (mol/mol)**	**K_{off} (s^{-1})**	**P/Lmax (mol/mol)**	**K_{off} [b] (s^{-1})**
HwTx-IV	0.01±0.01	N/A	negligible	N/A	0.03±0.05	N/A	0.05±0.01	N/A
mHwTx-IV	0.01±0.01	N/A	negligible	N/A	0.02±0.01	N/A	0.05±0.01	N/A
gHwTx-IV	0.07±0.02	95±11	0.16±0.03	75±5	0.05±0.01	89±3	0.11±0.01	76±4

[a] Peptide–lipid ratio (P/L mol/mol) calculated at the end of the association phase (t = 170 s) was plotted as a function of peptide concentration (0 – 64 μM) and fitted with Prism 7™ using one-site specific binding analysis; fitted P/Lmax and ± SE are shown; n = 3.

[b] K_{off} was calculated on Prism 7™ by fitting the data to an association then dissociation curve based on the 1:1 Langmuir binding equation at a fixed peptide concentration of 32 μM and assuming t_0 = 170 s (the point during the experiment when peptide injection was ceased); data is ± SE of the fitted parameters n = 3, K_{off} was not calculated for HwTx-IV or mHwTx-IV because the peptides showed minimal binding to the lipid bilayers studied.

Table 3. Net charge, surface accessible surface area (SASA) and residual dipole moments of HwTx-IV and gHwTx-IV

Peptide	Net charge[a]	Total SASA[b] (Å^2)	Polar SASA[b] (% of total SASA)	Apolar SASA[b] (% of total SASA)	Residual dipole moment[a] (Debye)
HwTx-IV	+4	3088.98	42.3%	57.7%	70.58
gHwTx-IV	+6	3019.41	37.9%	62.1%	80.76

[a] Net charge and residual dipole moment calculated using the g_dipoles tool on GROMACS

[b] SASA calculated using GETAREA: http://curie.utmb.edu/getarea.html.

Figure 1. HwTx-IV (PDB ID:2M4X) shown as a representative GMT. The peptide is colored by residue type with hydrophobic (green); positively charged (blue); negatively charged (red) and polar uncharged (white). (A) Ribbon representation of HwTx-IV with the inhibitory cystine knot (ICK) motif formed by three disulfide bridges (yellow) consisting of cysteine amino acid residues with the C1-C4, C2-C5, C3-C6 connectivity. (B) Surface representation showing the conserved hydrophobic patch and charged ring typically found in GMTs extracted from spider venom. (C) Sequence alignment of HwTx-IV, mHwTx-IV and gHwTx-IV. The sequences are aligned along the cysteine residues (bold black), amino acid modifications on mHwTx-IV and gHwTx-IV are underlined and * represents C-terminal amidation.

Figure 2. NMR analysis of HwTx-IV and its analogues. (A) Secondary Hα shift comparisons of synthetic HwTx-IV, mHwTx-IV and gHwTx-IV. The peptides showed good backbone alignment except at or near positions where mutations were present. Residue numbers of HwTx-IV and its analogues are shown on the x-axis. (B, C) NMR solution structure of gHwTx-IV (PDB ID: 5TLR). (B) The 20 best conformers as determined by lowest energy of minimization and highest MolProbity scores are superimposed with disulfide bridges shown in yellow. (C) Mutated residues (G1, G4, W33 and W6) of gHwTx-IV are shown in white.

Figure 3. Interactions of HwTx-IV and its analogues with model membranes. (A) Surface plasmon resonance sensorgrams obtained at peptide concentrations of 32 μM. Peptides were injected for 180 s onto lipid bilayers deposited onto the surface of a L1 chip. (B) Concentration–response curves obtained by plotting the amount of peptide bound to lipid (P/L mol/mol) at the end of peptide injection (t = 170 s) as a function of the peptide concentration (μM) injected over the lipid bilayer. All data points represent the mean (± SE) of three replicates. (C) Trp fluorescence emission spectra of 12.5 μM gHwTx-IV or HwTx-IV upon titration with a suspension of POPC/POPS (4:1) LUVs (0–4 mM). The fluorescence emission spectrum of HwTx-IV does not display a shift upon titration with lipid vesicles, whereas the fluorescence emission of gHwTx-IV showed a blue shift of 7 nm. (D) Quenching the Trp fluorescence emission intensity (excitation at 290 nm and emission at 350 nm) of 12.5 μM HwTx-IV, gHwTx-IV and L-Trp in the presence of 1 mM POPC/POPS (4:1) LUVs upon titration with acrylamide. The acrylamide quenching efficiency was

compared by fitting the data to the Stern-Volmer equation ($I/I_0 = 1$) and calculating the Stern-Volmer constant (K_{SV}) [40]. Acrylamide efficiently quenched the fluorescence emission of L-Trp ($K_{SV} = 49.1 \pm 2.5$ M^{-1}) and HwTx-IV ($K_{SV} = 48.4 \pm 1.2$ M^{-1}) in lipid vesicles. Fluorescence emission of gHwTx-IV was less efficiently quenched by acrylamide when in the presence of LUVs ($K_{SV} = 37.5 \pm 1.5$ M^{-1}) compared to buffer ($K_{SV} = 44.2 \pm 2.0$ M^{-1}); however, the small difference between gHwTx-IV K_{SV} values in lipid and buffer indicated a shallow positioning of the peptide in the membrane.

Figure 4. Inhibitory activity of HwTx-IV and its analogues at hNa$_V$1.7 in SH-SY5Y cells. Inhibition was monitored by following the fluorescence emission of the FLIPR calcium 4 dye. (A) Activation kinetics of HwTx-IV and the two analogues after activation by veratridine is shown at concentrations near the respective IC_{50} values of each peptide and at 1 μM. Activation was a measure of calcium influx into the cells. HwTx-IV, mHwTx-IV and gHwTx-IV inhibited the activation kinetics of hNa$_V$1.7 as is evidenced in their slower slopes of activation (HwTx-IV = 0.0196 ± 0.0006 fluorescence intensity/second; mHwTx-IV = 0.0143 ± 0.0003 fluorescence intensity/second; gHwTx-IV = 0.0257 ± 0.0009 fluorescence intensity/second) compared to veratridine (activation slope = 0.0609 ± 0.0026 fluorescence intensity/second). (B) Dose-response curves of HwTx-IV and of the two analogues are shown. Fluorescence emission data were normalized to the maximum and minimum signals for each peptide and data were fitted as F_{max} against concentration using a one-site specific binding curve with Hill slope. Data points are the mean ± SE (n = 4). Fitting of the dose–responses shows that gHwTx-IV is the most potent inhibitor ($IC_{50} = 7.55 \pm 1.54$ nM), whereas HwTx-IV ($IC_{50} = 32.4 \pm 4.74$ nM) and mHwTx-IV ($IC_{50} = 30.8 \pm 5.18$ nM) have similar inhibitory potencies. An apparent inhibition of hNa$_V$1.7 at low concentrations is evident on the curve and is a false positive effect often seen at low peptide concentrations.

Figure 5. Surface profiles and electrostatic surface potential profiles of HwTx-IV and gHwTx-IV. (A) Surface profiles of HwTx-IV (PDB ID: 2M4X) and gHwTx-IV (PDB ID: 5TLR) highlighting the positioning of E1, E4, F6 and Y33 on HwTx-IV and the corresponding mutations (G1, G4, W6 and W33) on gHwTx-IV. Peptides are colored by residue type including hydrophobic (green), positively charged (blue), negatively charged (red) and polar uncharged (white), showing a notable increase in the hydrophobic area of gHwTx-IV compared to HwTx-IV. (B) Electron density profiles of HwTx-IV and gHwTx-IV oriented to

show the face possessing the mutations on gHwTx-IV or corresponding native amino acids on HwTx-IV. gHwTx-IV has a more positive surface on the face possessing the four mutations compared to the equivalent face on HwTx-IV. Electron density distribution bars show a range from -5.0 (red) to +5.0 (blue).

Figure 6. Lipid interaction surface and channel binding region of gHwTx-IV. (A) Surface profiles of gHwTx-IV oriented to show that the hydrophobic patch possessing the four mutations (E1G, E4G, F6W and Y33W (green)) on gHwTx-IV is on a distinct face from the surface possessing the residues forming the channel binding region (K27, R26, and K32 (purple)) [12]. (B) An illustration of the voltage sensor domain II and pore of hNa_V1.7 channel is shown highlighting gHwTx-IV, the voltage sensor domain II, and the key residues identified as important for the activity of HwTx-IV (E811, D816 and E818) are underlined [12].

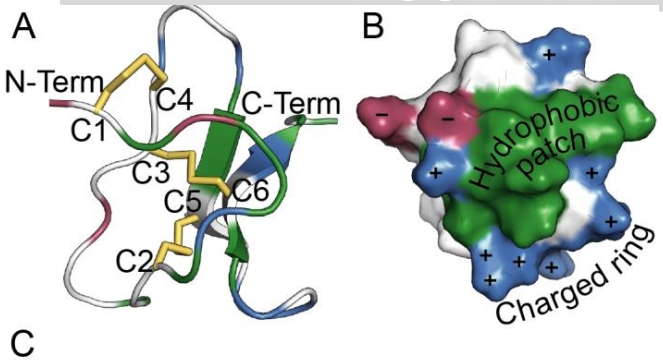

C

Peptide	Sequence
HwTx-IV	E**C**LEIFKA**C**NPSNDQ**CC**KSSKLV**C**SRKTRW**C**KYQI*
mHwTx-IV	PyrE**C**LEIFKA**C**NPSNDQ**CC**KSSKLV**C**SRKTRW**C**KYQI*
gHwTx-IV	G**C**LGIWKA**C**NPSNDQ**CC**KSSKLV**C**SRKTRW**C**KWQI*

Figure 1

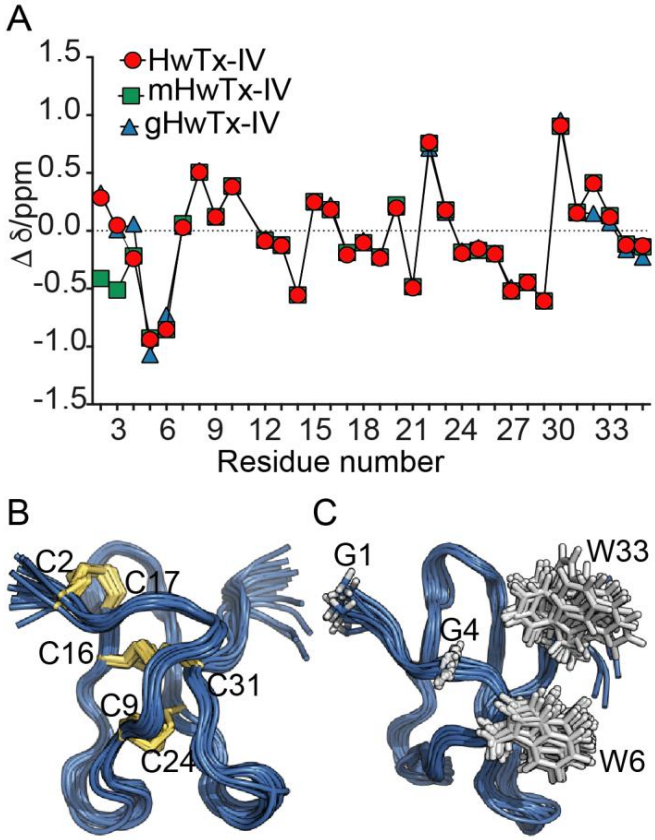

Figure 2

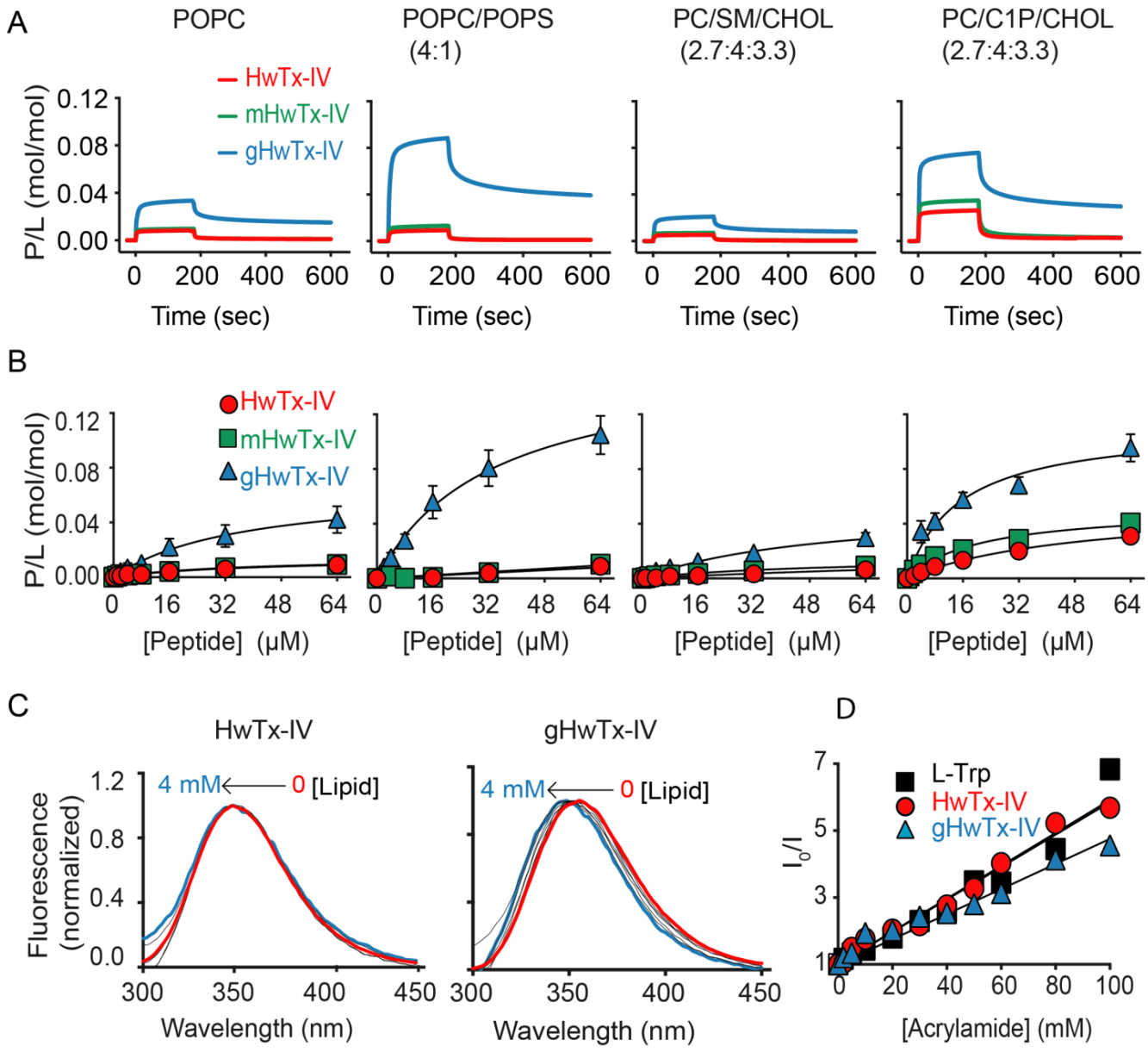

Figure 3

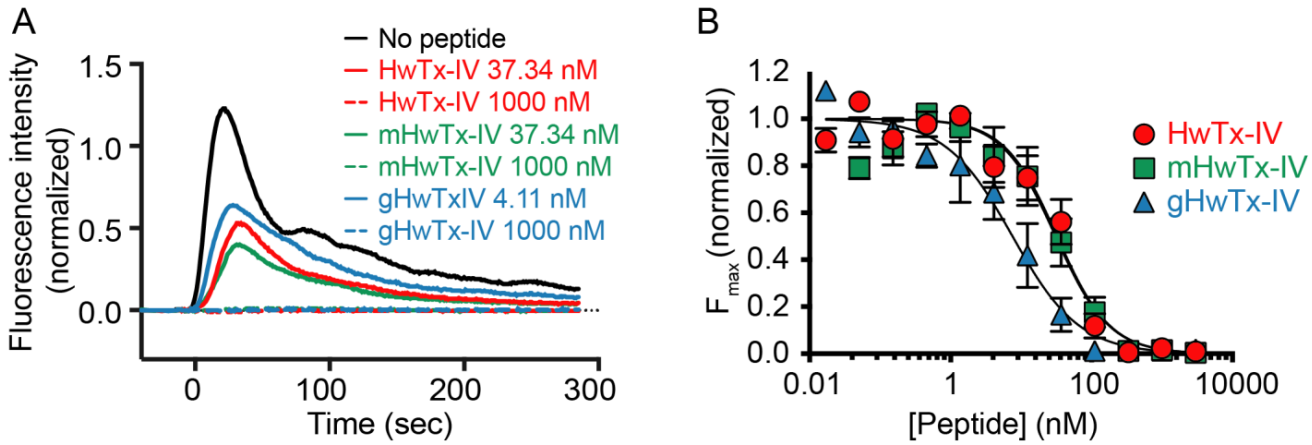

Figure 4

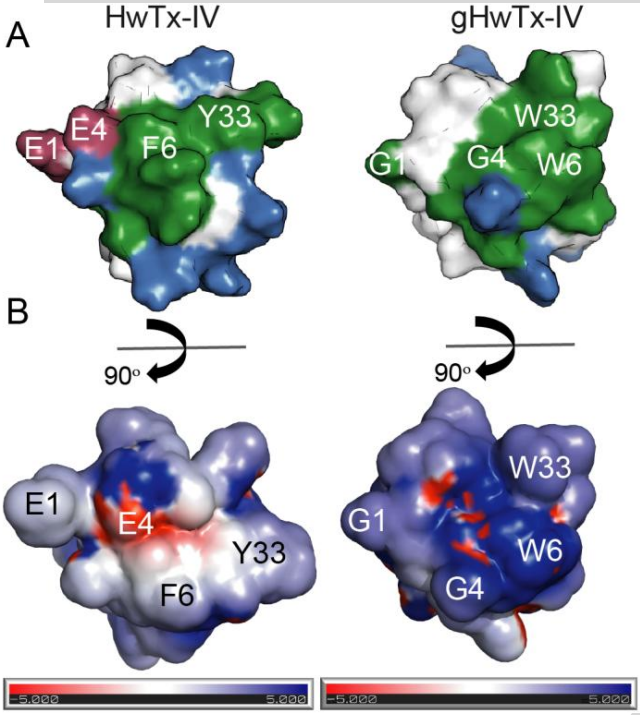

Figure 5

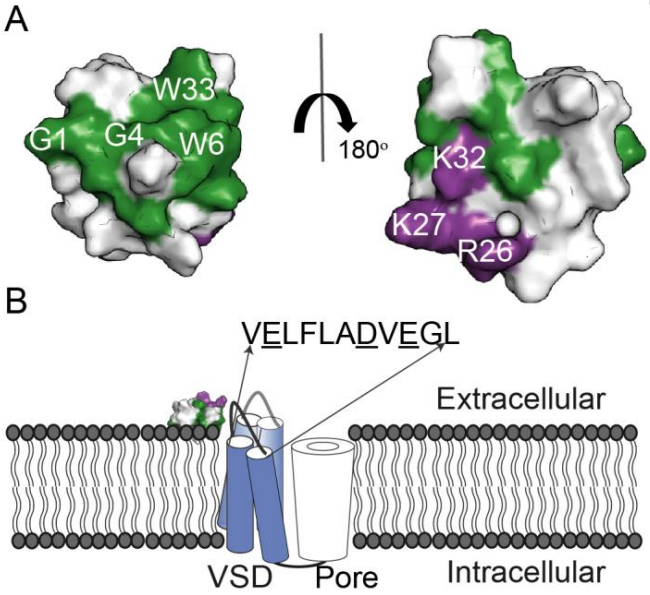

Figure 6

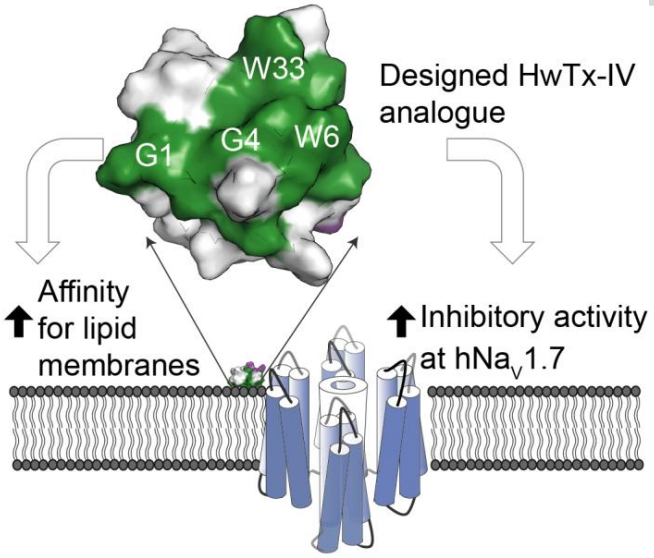

Graphical abstract